AFRL-AFOSR-UK-TR-2014-0022

Scattering Physics of Multistatic Radar Sea Clutter

Hugh Griffiths
Keith Ward

UNIVERSITY COLLEGE LONDON
GOWER STREET
LONDON WC1E 6BT UNITED KINGDOM

EOARD Grant 11-3062

Report Date: May 2014

Final Report from 1 October 2011 to 30 September 2013

Air Force Research Laboratory
Air Force Office of Scientific Research
European Office of Aerospace Research and Development
Unit 4515, APO AE 09421-4515

REPORT DOCUMENTATION PAGE

Form Approved OMB No. 0704-0188

1. REPORT DATE *(DD-MM-YYYY)*	2. REPORT TYPE	3. DATES COVERED *(From – To)*
30 May 2014	Final Report	1 October 2011 – 30 September 2013

4. TITLE AND SUBTITLE

Scattering Physics of Multistatic Radar Sea Clutter

5a. CONTRACT NUMBER

FA8655-11-1-3062

5b. GRANT NUMBER

Grant 11-3062

5c. PROGRAM ELEMENT NUMBER

61102F

6. AUTHOR(S)

Hugh Griffiths
Keith Ward

5d. PROJECT NUMBER

5d. TASK NUMBER

5e. WORK UNIT NUMBER

7. PERFORMING ORGANIZATION NAME(S) AND ADDRESS(ES)
UNIVERSITY COLLEGE LONDON
GOWER STREET
LONDON WC1E 6BT UNITED KINGDOM

8. PERFORMING ORGANIZATION REPORT NUMBER

N/A

9. SPONSORING/MONITORING AGENCY NAME(S) AND ADDRESS(ES)

EOARD
Unit 4515
APO AE 09421-4515

10. SPONSOR/MONITOR'S ACRONYM(S)

AFRL/AFOSR/IOE (EOARD)

11. SPONSOR/MONITOR'S REPORT NUMBER(S)

AFRL-AFOSR-UK-TR-2014-0022

12. DISTRIBUTION/AVAILABILITY STATEMENT

Distribution A: Approved for public release; distribution is unlimited.

13. SUPPLEMENTARY NOTES

14. ABSTRACT

This report presents work undertaken on Multistatic Radar Sea Clutter over the period October 2012 to April 2014. A number of topics have been addressed as follows: (1) NATO SET-185 is a research collaboration panel on sea clutter involving 9 nations. UCL has participated in collaborative work and meetings supported by this grant. (2) Low grazing angle sea clutter models. Differences between existing empirically derived models for average sea clutter backscatter have been investigated and compared with Propagation and EM scatter modeling. A number of potential explanations for the differences are proposed. (3) Multistatic radar measurement accuracy. The evaluation of measurement accuracy for a multistatic radar system is a difficult and complicated task. Work has been undertaken to derive a straightforward method, which is presented in this report.

15. SUBJECT TERMS

EOARD, multistatic radar, high grazing angles

16. SECURITY CLASSIFICATION OF:			17. LIMITATION OF ABSTRACT	18, NUMBER OF PAGES	19a. NAME OF RESPONSIBLE PERSON
a. REPORT	b. ABSTRACT	c. THIS PAGE			James H Lawton, PhD
UNCLAS	UNCLAS	UNCLAS	SAR	23	19b. TELEPHONE NUMBER *(Include area code)* +44 (0)1895 616187

Report on Scattering Physics of Multistatic Radar Sea clutter (EOARD grant FA8655-11-1-3062)

Keith Ward[1], UCL
October 2012 to April 2014

1. Summary

This report presents work undertaken on Multistatic Radar Sea Clutter over the period October 2012 to April 2014. A number of topics have been addressed as follows:

1. **NATO SET-185** is a research collaboration panel on sea clutter involving 9 nations. UCL has participated in collaborative work and meetings supported by this grant.

2. **Low grazing angle sea clutter** models. Differences between existing empirically derived models for average sea clutter backscatter have been investigated and compared with Propagation and EM scatter modelling. A number of potential explanations for the differences are proposed.

3. **Multistatic radar measurement accuracy**. The evaluation of measurement accuracy for a multistatic radar system is a difficult and complicated task. Work has been undertaken to derive a straightforward method, which is presented in this report.

2. Background

Maritime surface search radars have traditionally operated in a monostatic mode at low grazing angles when searching for small maritime targets such as periscopes and small boats. They have generally used a non-coherent, high bandwidth approach, which can be implemented in a small, lightweight design with low processing demands. A major reason for this operational choice of low grazing angles has been that the mean radar sea clutter return increases significantly at higher grazing angles (above about 10-15 degrees grazing), so that target radar signatures are masked by the large sea clutter returns. However, the requirements to cover wide surveillance areas to detect highly manoeuvrable target (utilised in suicide attacks, smuggling and piracy), and the use of high altitude radar platforms (jet aircraft and high altitude UAVs) have led to a need for radar systems operating at high grazing angles.

One potential way to overcome the sea clutter problem is to use a separate transmitter and receiver or receivers in a bistatic or multistatic configuration. Advances in RF technology and processing capacity have led to potential techniques to overcome the difficulties that have been traditionally associated with this approach. However, a lack of modelling in this area makes it difficult to quantify the levels of performance that could be expected. UCL has been undertaking multistatic measurements using the NetRad radar, which has produced data suitable for comparison with EM modelling. Most of this data is at low grazing angles due to the transmitter and receivers being located on the land looking out to sea. Thus it has been important to develop modelling that includes low grazing angles.

In the previous report on this project [1] a description was given of an EM scattering model, which is suitable for comparison with existing data sets and other published scattering models. The model uses Physical Optics at high grazing angles, a two scale composite model at medium grazing angles, and an enhanced composite model (with multipath and breaking waves) at low grazing angles. The model has been implemented for a 3D (2D and wave height) stochastic model for the ocean surface, at radar frequencies of 10 GHz, 16 GH and 35

[1] With acknowledgement to my colleagues Robert Hill and Robert Tough for their assistance with the work on Propagation and Measurement Accuracy respectively.

GHz and grazing angles from 0.1 to 90 degrees. This model can in principal be used in monostatic and multistatic configurations, although much of the multistatic geometry has not yet been implemented in the model.

Comparison of the model results with monostatic data highlights that there are large differences between existing published monostatic models based on experimental data. The changes that occur when moving from monostatic to bistatic geometries turn out to be smaller that existing discrepancies between the different sets of published monostatic data. Therefore little progress can be made on the bistatic case until we understand why the monostatic data models are so different. This topic is addressed here in section 4.

One potential benefit of multistatic radar systems is their ability to locate and track targets more accurately than equivalent monostatic systems. However, quantification and analysis of this benefit is generally very complicated and mathematical. In order to allow straightforward comparisons to be made, we have developed a simple method of deriving the accuracies using Gaussian error modelling and techniques similar to those used in the derivation and application of Kalman filters. The analysis might be familiar to specialists in multilateration and multi-sensor tracking, but not perhaps to radar engineers. Our work is described here in section 5.

The maritime 'high grazing angle problem' described above is of interest to many nations. A NATO Set panel has therefore been set up to address this issue and we are participating in it as part of this project. A summary of the activities of SET-185 is therefore give below in section 3.

3. NATO SET Panel 185

The NATO SET-185 panel has met five times:

NATO, Paris	January 2012
FGAN, Germany	May 2012
Thales, UK	February 2013
ONERA, France	September 2013
NRL, USA	March 2014

The following individuals associated with UCL have been involved in these meetings (not all at all meetings):

Professor Hugh Griffiths
Professor Simon Watts (UCL visiting professor)
Professor Keith Ward (UCL visiting professor)
Matthew Ritchie, PhD student

The panel has representatives from Canada, USA, Germany, France, UK, Turkey, Australia, Norway and the Netherlands. It was been set up to collaborate on different approaches to overcome the high grazing angle problem. The programme of research being undertaken by the SET Panel takes advantage of a wide range of sources of real radar data provided by the participants. It concentrates on analysing this data, developing empirical models for clutter & targets, and assessing detection schemes using the observations and the results of data analysis. The panel recognises the potential value of physical models of sea clutter and so a small team within the panel is undertaking a program of EM scattering calculations and modelling to underpin the data analysis and detection work.

Presentations made by UCL at the five meetings covering sea clutter data analysis, statistical modelling, simulation, coherent detection analysis and EM scattering may be found on the NATO SET SharePoint.

4. Low grazing angle reflectivity of sea clutter

4.1 Models derived from measured data

Recently a report was published by Gregers-Hansen and Mital [2] re-examining the tables of sea clutter RCS published by Nathanson [3]. They make the powerful point that the tabulated data is collated from approximately 60 sources and 'probably represents the most complete data base of sea clutter reflectivity available to the radar systems engineer'. In the report curve fitting is used to produce a mathematical expression to approximate the functional dependence of the data in the tables (i.e., the variation with grazing angle, radar frequency, polarisation and sea state). The formula is then proposed as an empirical model (the 'NRL model') for use by radar system engineers. A similar exercise was undertaken in the UK in the 1970's at the Royal Radar Establishment [4] for X-band using the tables in an earlier edition of Nathanson. This earlier work was designated the 'RRE model', was widely used for radar specification and assessment in the UK, but was not published in the open literature until it was presented in a book by Ward, Tough and Watts [5].

There is also a widely used sea clutter model proposed by Horst et al [6], and known as the 'GIT model', which has found wide acceptance in the radar community. In the NRL report [2] it is pointed out that the GIT model does not always agree with the tabulated Nathanson data. The discrepancies are quite large, especially at low sea states, and can, according to reference [2], lead to overly optimistic radar performance predictions. Although the GIT model is based on measured sea clutter data, records do not appear to exist listing the data sources and analysis techniques employed. As the work was done in the 1970's it is probably not practical to reconstitute the data. I was told by workers from Georgia Tech after the work was done that great care was taken to exclude data from measurement environments with non-standard atmospheric propagation, as this can distort results at low grazing angles in the Nathanson tables.

Plots of the clutter reflectivity for the three models (NRL, RRE and GIT) are shown in Figures 1, 2 and 3 for a radar frequency of 9 GHz, grazing angles between 0.1° and 10°, and sea states 1 to 5. It is clear that the NRL and RRE models are similar (as they should be, since they are based on some of the same data), whilst the GIT model has much smaller values of reflectivity at low sea states and grazing angles, as discussed above.

Our work [5] has been mainly on the statistical fluctuations of sea clutter, but when we have analysed the average reflectivity we have usually found the GIT model to be the most accurate representation of the data. Unfortunately, collecting and calibrating sufficient sea clutter data to derive trends over grazing angles, sea states, polarisations and radar frequencies constitutes a very significant task, which we have never been able to undertake. Thus we do not have sufficient data to compare with all of Nathanson's trends, except in a few special cases. One such case is shown in figures 4 and 5. Here, the clutter reflectivity measured by an airborne radar system, flying at an altitude of 500 feet, is plotted versus range. The data collection patch is set when the radar is at long range and is then geographically stabilised as the aircraft flies in. This means that same physical patch of sea is measured at different grazing angles, and thus the measurement excludes any effects of the spatial variation of weather or oceanography. The clutter data is corrected for the effects of receiver noise, which can otherwise enhance the apparent reflectivity at long range (i.e., at low grazing angle). In figure 4 the data is compared with the RRE sea clutter model [4] derived from the Nathanson tables, and in figure 5 the data is compared with the GIT clutter model [6]. The fluctuations in the black data line indicate the measurement accuracy obtained from estimations using short range and time extents of spiky sea clutter data.

The data shows that, if the Nathanson tables were to be used to estimate the sea state from the data, then the result would be sea state 1 at long range (low grazing angle) and sea state 6 at short range (high grazing angle). Clearly in the 10 minutes it took the aircraft to collect the data the sea state could not have changed to this degree. It the GIT model were to be used, an estimate of sea state 3 would result at all the grazing angles. Thus we must conclude that for this data the GIT model is much more accurate in its representation of the effect of grazing angle change than either the RRE or NRL models.

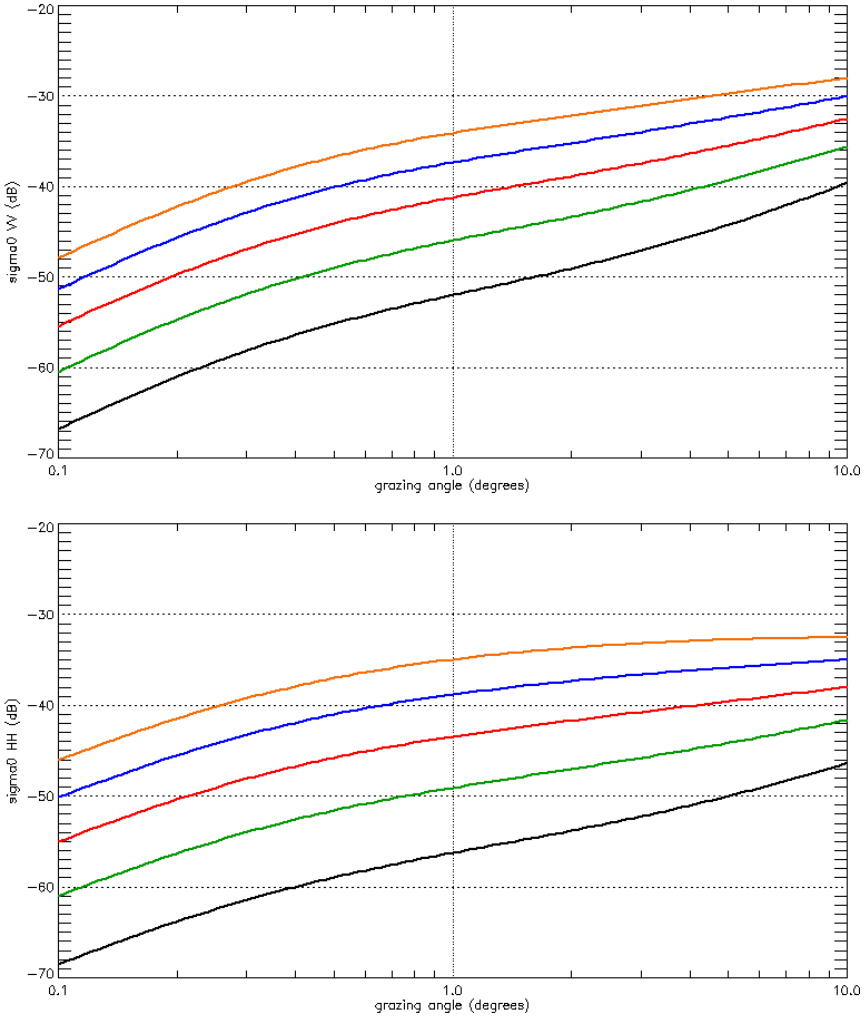

Figure 1: *NRL model [2] of Sea clutter normalised RCS at 9 GHz versus grazing angle for sea states 1 to 5 (top graph is VV lower graph is HH)*

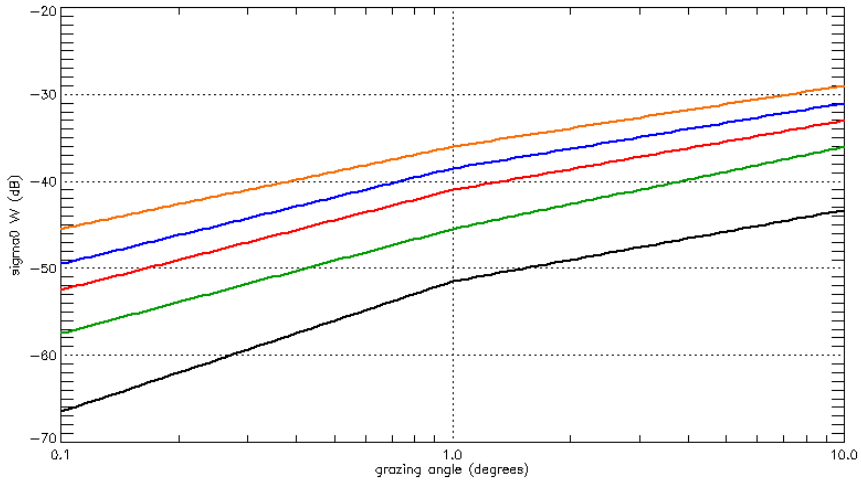

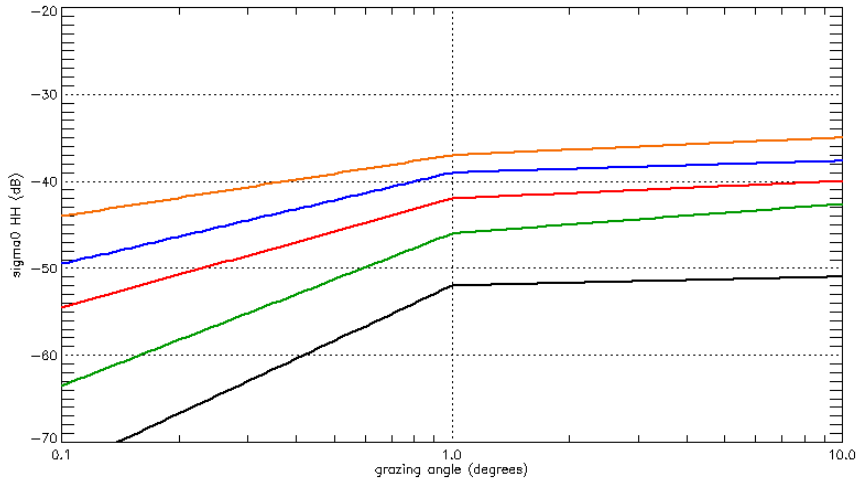

Figure 2: *RSRE model [4] of Sea clutter normalised RCS at 9 GHz versus grazing angle for sea states 1 to 5 (top graph is VV lower graph is HH)*

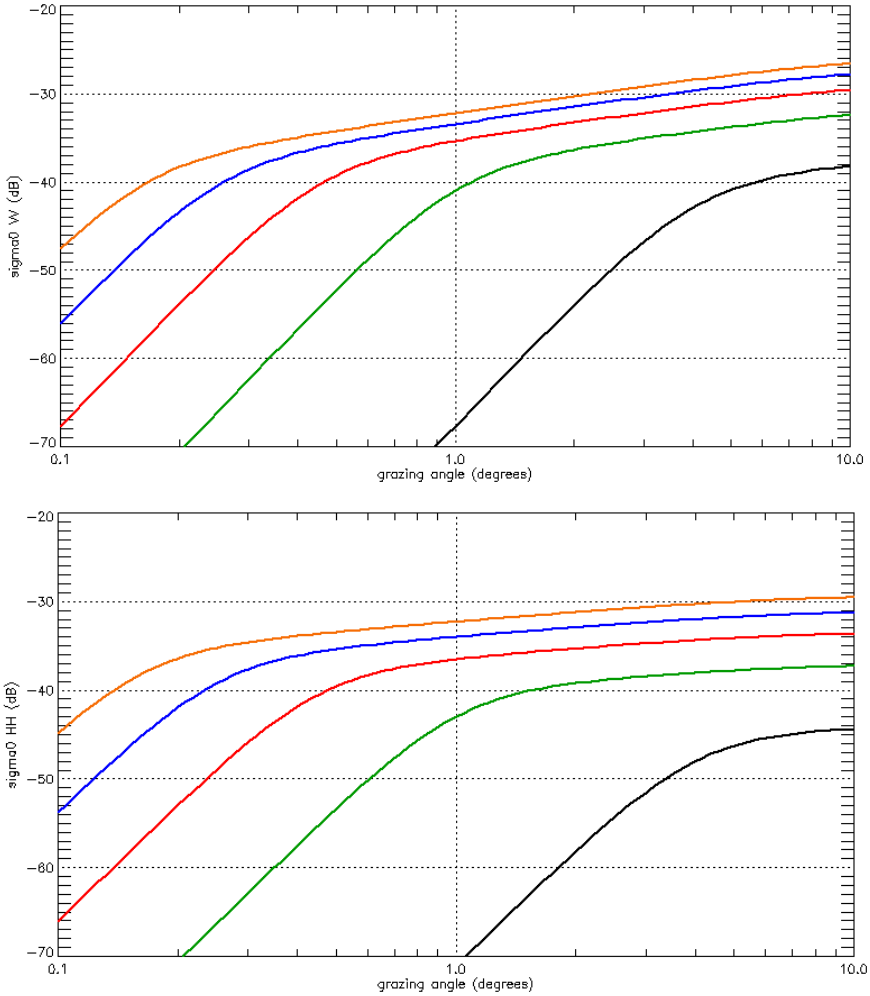

Figure 3: *GIT model [6] of Sea clutter normalised RCS at 9 GHz versus grazing angle for sea states 1 to 5 (top graph is VV lower graph is HH)*

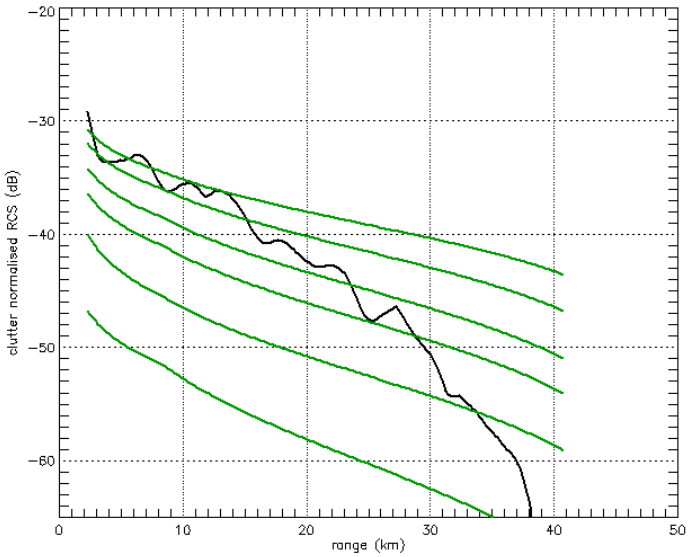

Figure 4: *Sea clutter normalised RCS measured at 9.75 GHz from an aircraft at 500 feet altitude (black line) compared with the RRE sea clutter model [4] (green lines corresponding to sea states 1 to 6)*

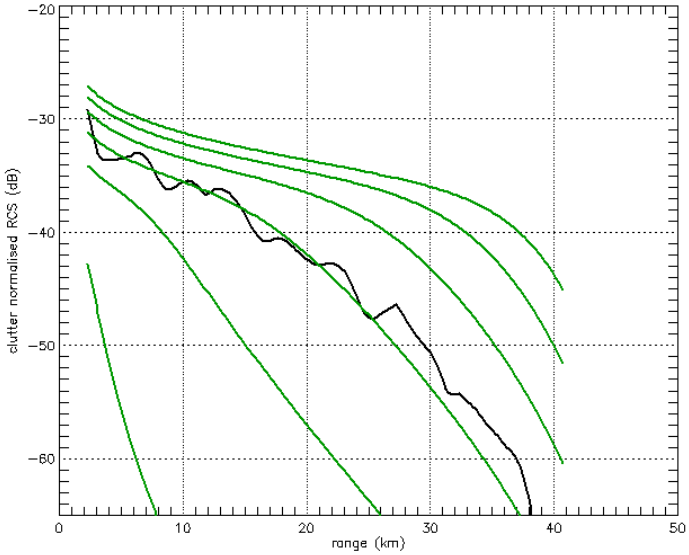

Figure 5: *Sea clutter data as plotted in figure 5 (black line) compared with the GIT sea clutter model [6] (green lines corresponding to sea states 1 to 6)*

As discussed above, we do not have sufficient data of the type plotted in figures 4 and 5 to provide a 'measured data' alternative to the Nathanson tables, but on the other hand we cannot disregards the experience over the past twenty years that has led workers round the world to adopt the GIT model as the best fit to their data. So we need to consider potential explanations for biases in the Nathanson tables. Much of the data is very old and was collected when A to D converters, digital recording and computer analysis equipment were much inferior to today, thus making it difficult to do direct analysis of large quantities of data. Possible sources of bias include:

1. The effects of spiky sea clutter.
2. Lack of correction for system noise.
3. Anomalous propagation and the effect of propagation on the local grazing angle.

Below we consider some of these, and scattering physics results that contribute to the choice of reflectivity model.

4.2 Electromagnetic scattering calculations

Modelling the electromagnetic backscatter from the sea surface is a difficult undertaking due to the nature of the equations governing the shape of the sea surface and the reflection of the EM waves at the boundary between the air and sea water. There are many approximations and techniques that attempt to solve the problem, but at low grazing angles the best we can currently do is to use numerical techniques to solve the integral equations. Examples of the various approximations and techniques are given in [5]. Here we describe some numerical results that demonstrate behaviour similar to the GIT model for reflectivity versus grazing angle.

The first step is to generate random surfaces with an ocean-like wave spectrum. An example is shown in figure 6. The red lines on the plot are rays illuminating the surface at a grazing angle of three degrees. Shadow regions are evident where the long waves obscure parts of the surface from the rays.

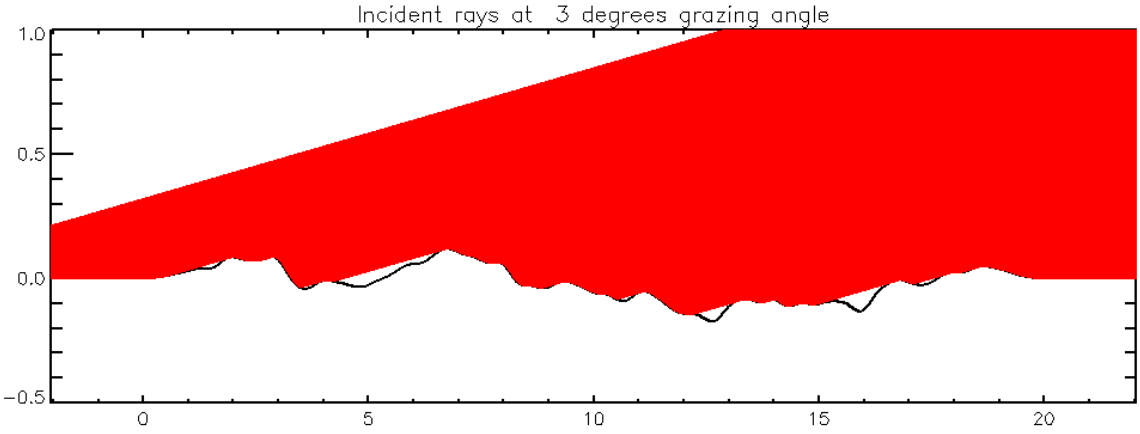

Figure 6: *An ocean-like surface (x and y axes in metres) illuminated with rays at 3 degrees grazing angle.*

One approximation for scattering is the Composite Model (described in [1]) where this ray-like illumination of the long waves is scattered back by small scale roughness riding on the long waves. The backscattered power is calculated using small perturbation theory, which is applied to each area on the long waves, assuming that the long wave structure can be approximated by a plane at a tangent to the long wave structure at that point (the so-called tangent plane approximation). The scattered power versus range from the surface is plotted in Figure 7. The shadowed regions can be seen as gaps in the backscattered power profile.

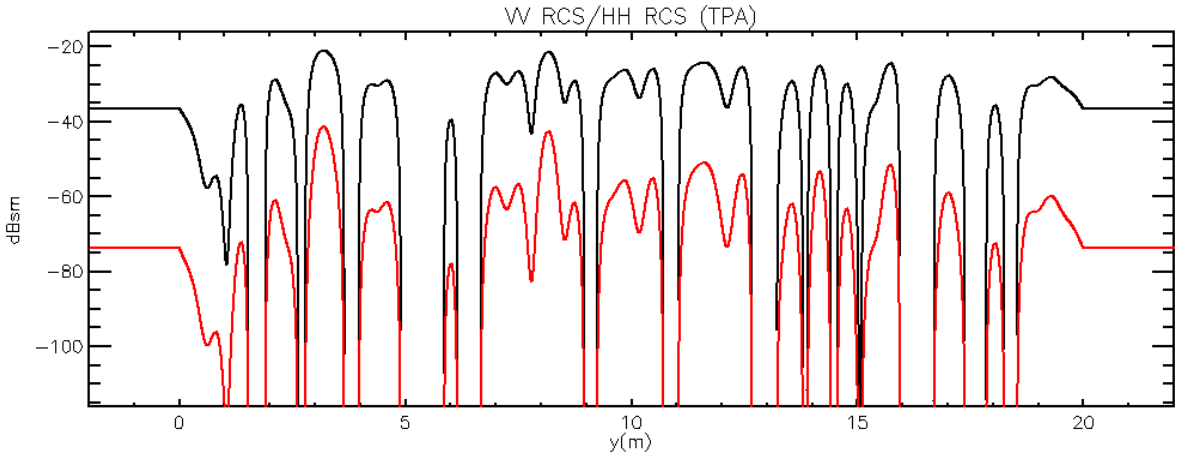

Figure 7: *Backscattered power versus range for the composite model applied to the surface in Figure 6. The black line is VV polarisation and the red line is HH*

The composite model may be improved considerably by relaxing the ray approximation to the illumination of the long wave structure and applying Forward-Backward [7], sometimes called the 'method of ordered multiple interactions', to the smooth surface profile. This numerical technique solves the integral equations for the EM fields on the surface of the smooth surface, and in the process accounts for the multiple scattering and diffraction that is omitted from the ray calculation. The small scale roughness is then added by perturbing the smooth surface fields using the Lorentz Reciprocity Principle (described in [8]). The resulting backscattered power versus range is plotted in figure 8, where is can be seen that the multiple scattering and diffraction has filled in the shadow regions of figure 7.

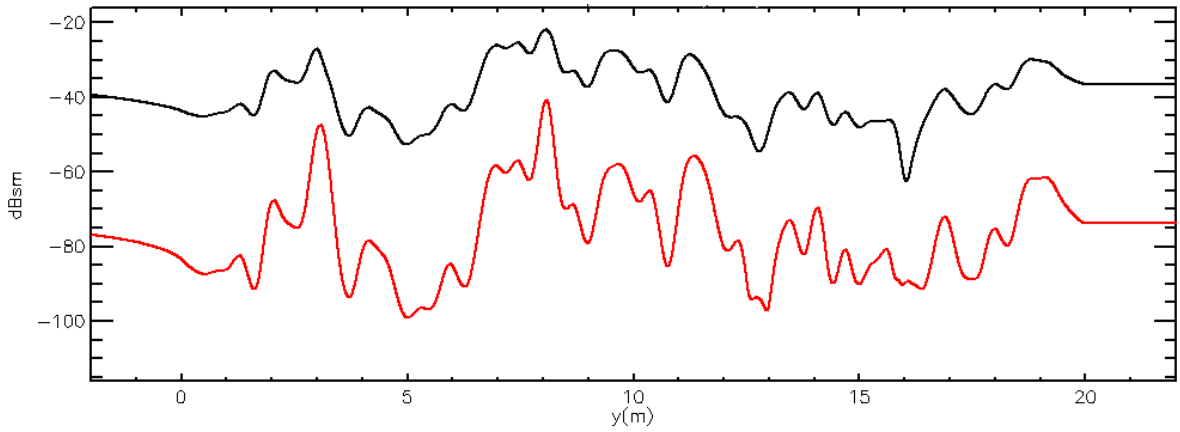

Figure 8: *Backscattered power versus range for the FB and LRP applied to the surface in Figure 6. The black line is VV polarisation and the red line is HH*

When the power is summed over range, averaged over many surface realisations and recalculated at various grazing angles and rms sea surface wave heights, trends of reflectivity versus grazing angle and sea state emerge. These are plotted in figure 9 (on an arbitrary scale of reflectivity). The behaviour versus sea state and grazing angle of the back curves, which include multiple scattering, is very similar to the GIT model but different from the NRL and RRE models. This shows a strong connection between physical scattering modelling and the GIT empirical model.

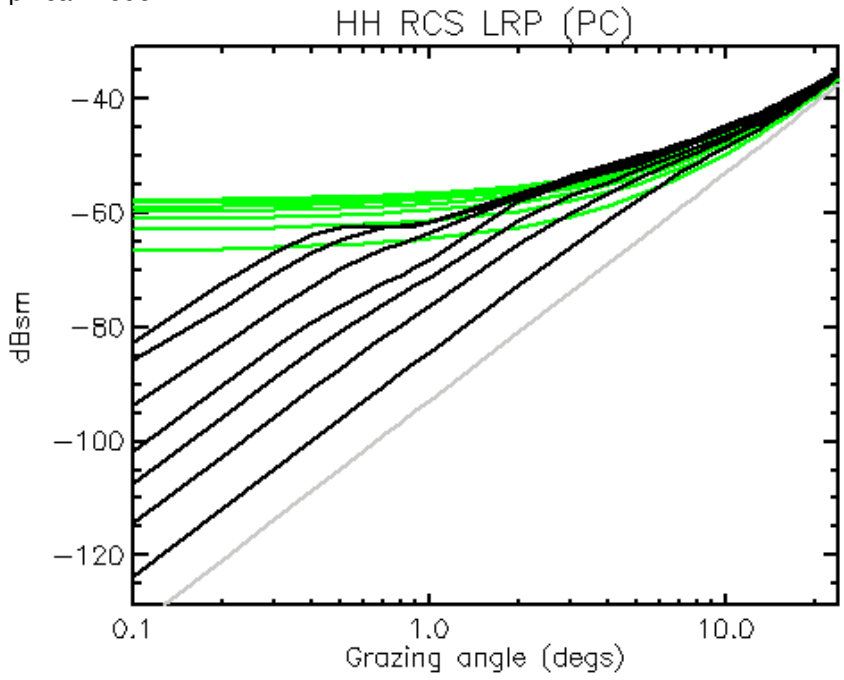

Figure 9: *Average RCS for scattering from an ocean-like surface derived using the Forward-Back (FB) method. The black lines correspond to FB & LRP, the green lines to the 'composite model' and the grey line corresponds to the SPM or Rice result .*

4.3 Propagation modelling and local grazing angle

As discussed in section 4.1, atmospheric propagation can have a significant effect on the apparent sea clutter reflectivity. The modelling discussed above in 4.2 assumes that the sea is illuminated by the radar with a plane EM wave propagating in the direction of the line-of-sight of the radar. In reality the atmosphere 'bends' the waves due to altitude variations of refractive index. For normal conditions (the Standard Atmosphere) this can be accounted for by using a 4/3 Earth radius in the calculation of grazing angle.

Models for sea clutter reflectivity are designed to apply only to illumination through the Standard Atmosphere. Any data from conditions of anomalous propagation should be excluded from data sets used to test models, and should be subjected to specific propagation modelling. Most radar systems engineers adopt this approach (although there is some doubt that the Nathanson data tables excluded anomalous propagation data). However, there is a suggestion by some that the grazing angle for a standard atmosphere does not go below a non-zero limiting value, and this accounts for the higher reflectivity at low grazing angles for the Nathanson data tables than EM calculations. Here we explore this hypothesis and conclude that, if there is a limiting grazing angle, it too low (<0.05°) to account for the discrepancy. Also, it is most likely that the limiting grazing angle is a computational artefact, resulting from trying to model illumination in a shadow as an incoming plane wave (as one might do, for instance, with the Geometric theory of diffraction, GTD).

In propagation modelling a standard simplifying assumption is of a horizontally stratified atmosphere. Microwave propagation in the troposphere (~0-17 km) is dominated by the effects of atmospheric refraction which are dependent on environmental conditions. The average value of the refractive index at the earth's surface is close to 1 (a figure of n =1.000315 is given by the ITU as representative for mid-latitudes). A convenient quantity related to the refractive index is the refractivity, which is defined as

$$N = (n-1)10^6 \tag{4.1}$$

In standard conditions, the refractive index decreases with height and can be described by an exponential model, [90.

$$N = N_0 \exp\left(-\frac{h}{h_0}\right) \tag{4.2}$$

where h is the height above sea level, N_0 = 315 and h_0 = 7.35 km. At low altitudes this is well approximated by a linear model. The US standard atmosphere is defined by the alternative parameters N_0 = 316 and h_0 = 8.08 km.

Refraction at the boundary of two uniform media is described by Snell's law

$$n_1 \sin\theta_1 = n_2 \sin\theta_2 \tag{4.3}$$

where θ is the angle measured from the normal of the boundary. When the refractive index is a continuous function of height the rays curve and are described by

$$n \sin\theta = n_0 \sin\theta_0 \tag{4.4}$$

The above expressions assume a flat earth and must be modified to take into account the earth's curvature. If the plane boundaries separating regions of constant refractive index are replaced by spheres as shown in Figure 10 then consideration of the triangle OAB gives

$$r_1 \sin\theta_1 = r_2 \sin x \tag{4.5}$$

Then the application of Snell's law at the upper boundary leads to

$$n_1 r_1 \sin\theta_1 = n_2 r_2 \sin\theta_2 \tag{4.6}$$

In the case of a continuously stratified atmosphere we obtain

$$nr \sin\theta = n_0 r_0 \sin\theta_0 \tag{4.7}$$

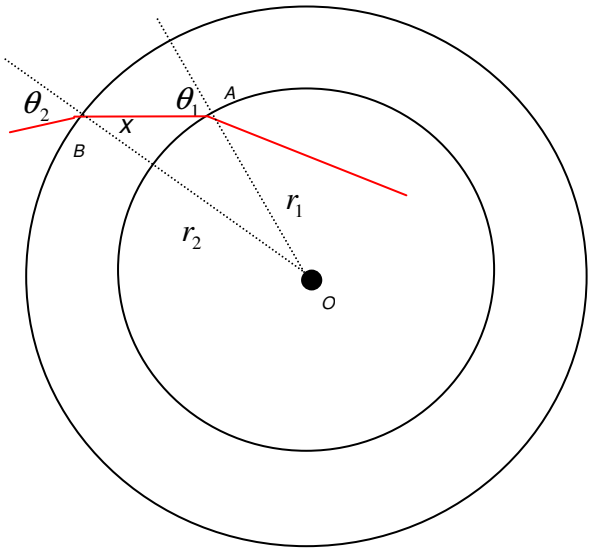

Figure 10: *Sketch of spherical geometry*

The standard 4/3 earth model used in radar performance calculations is obtained by letting $r = r_0 + h$ where h is small compared with r_0 and considering a linear refractive index gradient $n = n_0 + \frac{dn}{dh} h$. Using the fact that n_0 is very close to 1 we obtain

$$\sin\theta_0 = \left(1 + h\left(\frac{1}{r_0} + \frac{dn}{dh}\right)\right)\sin\theta \tag{4.8}$$

showing that a linear gradient of refractive index has the same effect on refraction as the curvature of the earth. The effect of refraction can be accounted for by using an effective earth radius of kr_0 where

$$k = \frac{1}{1 + r_0 \dfrac{dn}{dh}} \tag{4.9}$$

When the refractivity gradient of -39 N/km corresponding to the US standard atmosphere is used the traditional value of 4/3 is recovered. The curvature can therefore be introduced using a modified refractive index, *m*

$$m(x,z) = n(x,z) + \frac{z}{a} \tag{4.10}$$

A modified refractivity, M, is defined as

$$M = (m-1)10^6 \tag{4.11}$$

In a standard atmosphere M increases approximately linearly with height. In the presence of evaporation ducts, which lead to anomalous propagation, M first decreases with height then increases.

The parabolic equation for radio-wave propagation was first developed by Leontovich and Fock in the 1940s [10]. Parabolic equation techniques have been widely used for radiowave propagation modeling since the mid-1980s and are now the method of choice for radar propagation modeling. A detailed description of the method and its numerical implementation is given in [11] and [12].

It is worth recalling that the wave equation is

$$\frac{\partial^2 f}{\partial t^2} = c^2 \nabla^2 f \tag{4.12}$$

The associated Helmholtz equation is obtained by removing the $\exp(-i\omega t)$ to obtain

$$\nabla^2 \psi + k^2 \psi = 0 \tag{4.13}$$

and the definition of the refractive index gives $k = k_0 n$ where k_0 denotes the wavenumber for propagation in free space.

We consider waves propagating in the x-direction with fields independent of the transverse y coordinate. This is described by the scalar Helmholtz equation (4.13), with $\psi(x,z) = E_y(x,z)$ in the case of horizontal polarization and $\psi(x,z) = H_y(x,z)$ for vertical polarization. The paraxial wave equation is obtained by writing

$$u(x,z) = e^{-ikx}\psi(x,z) \tag{4.14}$$

To obtain

$$\frac{\partial^2 u}{\partial x^2} + 2ik\frac{\partial u}{\partial x} + \frac{\partial^2 u}{\partial z^2} + k_0^2\left(n^2 - 1\right)u = 0 \tag{4.15}$$

The standard parabolic equation is obtained by neglecting the $\frac{\partial^2 u}{\partial x^2}$ term. A detailed analysis considers a factorisation into forward and back propagating waves and a Taylor expansion of a pseudo-differential square root operator. The parabolic equation model which describes forward propagating waves at small angles from the paraxial direction is

$$\frac{\partial^2 u}{\partial z^2} + 2ik\frac{\partial u}{\partial x} + k_0^2\left(n^2 - 1\right)u = 0 \tag{4.16}$$

In order to introduce the effect of a curved Earth, n for a standard atmosphere is replaces in (4.16) by m as defined in equations (4.10) and (4.2). A widely used model for the behavior of the modified refractivity in the presence of an evaporation duct is described in [13]. The model is

$$M(z) = M_0 + 0.125z - 0.125\delta \ln\left(\frac{z + z_0}{z_0}\right) \tag{4.17}$$

where z is the height above mean sea level (m), δ denotes the evaporation duct height (m) and z_0 is an aerodynamic roughness parameter whose typical value is $1.5\text{x}10^{-4}$ m. M_0 is the modified refractivity at the surface which has a typical value of between 300 and 350.

The calculation of radio wave propagation over the ocean surface has thus been reduced to the numerical solution of the parabolic equation

$$\frac{\partial^2 u}{\partial z^2} + 2ik\frac{\partial u}{\partial x} + k_0^2\left(m^2 - 1\right)u = 0 \tag{4.18}$$

together with the appropriate initial and boundary conditions. The boundary conditions at a perfectly conducting surface are Dirichlet (u = 0) for horizontal polarisation and Neumann ($\frac{\partial u}{\partial z} = 0$) for vertical polarisation. The numerical solution of the parabolic equation includes a maximum height and this needs to be dealt with to ensure that no unphysical reflections occur at the top of the computational domain. The initial conditions require a description of the source of the radio waves.

The split step method propagates the solution outwards via Fourier transforms. The Fourier transform pair is given by

$$\begin{aligned} \tilde{u}(x,p) &= \int_{-\infty}^{\infty} u(x,z)e^{-i2\pi pz}dz \\ u(x,z) &= \int_{-\infty}^{\infty} \tilde{u}(x,p)e^{i2\pi pz}dp \end{aligned} \tag{4.19}$$

In the case of a constant refractive index, the Fourier transform of the parabolic equation gives

$$\tilde{u}(x,p) = \exp\left(\frac{i}{2}k_0\left(m^2 - 1\right)x\right)\tilde{u}(0,p)\exp\left(-i\frac{2\pi^2 p^2 x}{k_0^2}\right) \tag{4.20}$$

In the absence of a reflecting surface the convolution theorem can be applied to obtain

$$u(x,z) = \sqrt{\frac{k_0}{2\pi x}}e^{-\frac{i\pi}{4}}\exp\left(-\frac{ik_0 x\left(m^2 - 1\right)}{2}\right)\int_{-\infty}^{\infty} u(0,z')\exp\left(\frac{ik_0(z-z')^2}{2x}\right)dz' \tag{4.21}$$

When the refractive index varies with height a split step algorithm is employed which is motivated by the Fourier transform result above and justified using the formal manipulation of differential operators. This results in the stepping procedure

$$u(x+\Delta x,z) = \exp\left(\frac{ik_0\left(m^2(z)-1\right)\Delta x}{2}\right)F^{-1}\left(\exp\left(\frac{-i2\pi^2 p^2\Delta x}{k_0}\right)F(u(x,z))\right) \tag{4.22}$$

The calculation of propagation is implemented by marching out from the source to the maximum range of interest. The sampling required in the z-direction is related to the angle of propagation as $p = k\sin\theta$. Substituting a plane wave of the form

$$\begin{aligned} \psi &= \exp(i(xk_x + zk_z)) \\ u &= \exp(i(x(k_x - k) + zk_z)) \end{aligned} \tag{4.23}$$

into the parabolic equation gives

$$\begin{aligned} k_z^2 &= 2k(k - k_x) \\ (\cos\theta - 1)^2 &= 0 \end{aligned} \tag{4.24}$$

which shows that errors occur when the angle of propagation differs from the paraxial direction.

The vertical sampling is based on the definition of a maximum propagation angle, $\theta_{\max}$, in the region of 5 to7 degrees then

$$\Delta z = \frac{1}{2k\sin\theta_{\max}} = \frac{\lambda}{4\pi\sin\theta_{\max}} \tag{4.25}$$

The sampling in the x direction is less critical and a value of *dx* = 100 m has been used. The computational domain for a perfectly conducting boundary is shown in Figure 11 below.

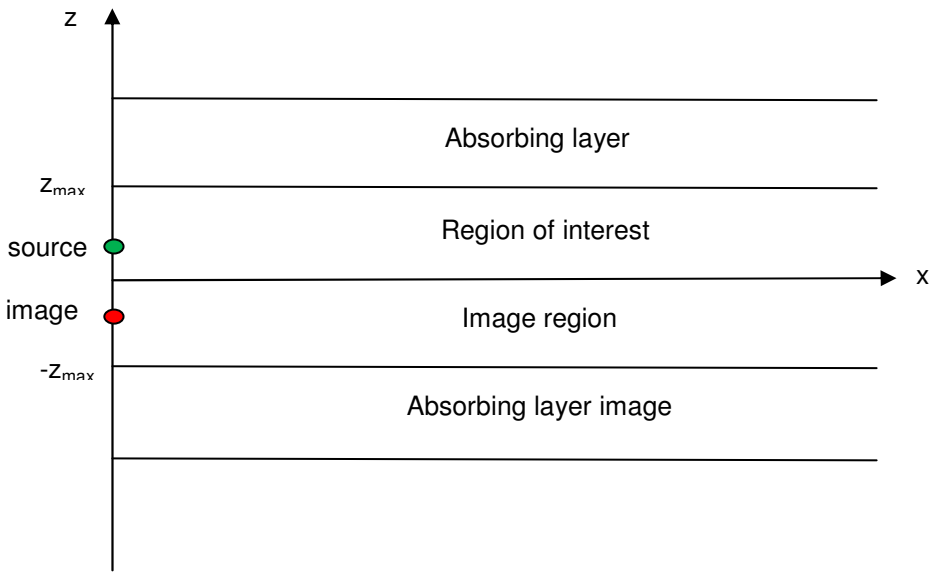

Figure 11: *Sketch of propagation computational domain*

The initial field is defined in the fourier domain using the method of images to satisfy the boundary conditions at the (flat) surface. The expression below describes a Gaussian beam pattern with beam width β. The parameter *s* is -1 for horizontal polarisation and 1 for vertical polarisation. The antenna elevation angle is given by the parameter *e*. The initial field is obtained by taking the inverse Fourier transform

$$\begin{aligned} u &= F(p)\left(\exp(-i2\pi p h_r) + s\exp(i2\pi p h_r)\right) \\ F(p) &= \exp\left(-4\ln(2)\frac{\varphi(p)^2}{\beta^2}\right) \\ \varphi(p) &= \sin^{-1}\left(\frac{p}{k} - \sin(e)\right) \end{aligned} \tag{4.26}$$

The modified refractive index in the region [0, *zmax*] is calculated using either the standard atmosphere model of equation **Error! Reference source not found.**4.2) (with a curved earth correction added) or the duct model of equation (4.17). This is extended into the absorbing layer where an imaginary component is added to m^2; the imaginary component has the form

$$\mathrm{D} = \begin{cases} 0 \ \text{ for } 0 < z < z_{\max} \\ iH(z)\varepsilon \text{ for } z > z_{\max} \end{cases} \tag{4.27}$$

where H represents a Hanning weighting that is zero when $z = z_{max}$ and increases to 1 when $z = 2z_{max}$. The quantity $\varepsilon = 0.0001$. This form ensures there is no discontinuity at the boundary and avoids spurious reflections. The refractive index is extended to the image domain by reflection.

The refraction and spreading exponentials in the stepping algorithm are both independent of x and can be pre-calculated outside the propagation loop.

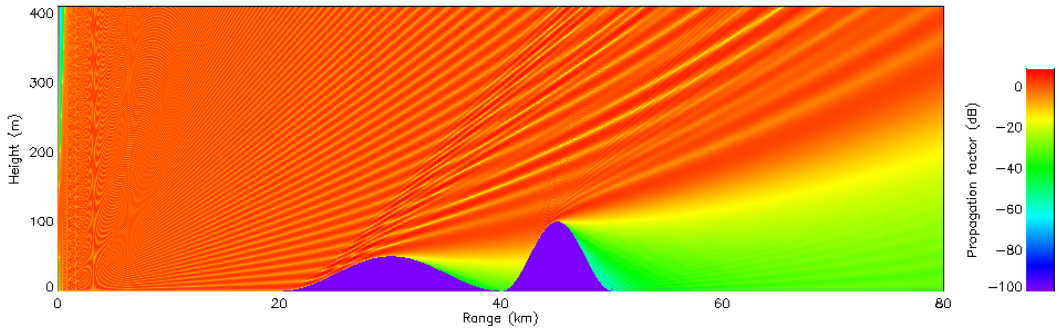

Figure 12: *Propagation factor versus range and height for an antenna height of 100m, 3GHz RF frequency, a curved Earth and a standard atmosphere*

This calculation gives the propagation factor above the surface, and can be used in radar performance calculations to assess the impact of propagation on target returns. An example is shown in Figure 12, where a couple of terrain bumps are included to demonstrate interference caused by multipath. (The method of incorporating terrain in the Split Step method is described in [12]). Other quantities required in radar performance calculations are the surface propagation factor modulating clutter returns and the grazing angle of incident waves. The method of images approach ensures that the propagation factor at the surface is zero for horizontal polarisation. In order to derive a surface propagation factor the effects of incident and reflected waves must be separated.

This is done by applying the following steps

- Fourier transform the field u;
- Set the components with positive frequencies to zero
- Inverse Fourier transform to obtain $\hat{u}(z)$

The surface propagation factor is the obtained from $\hat{u}(0)$. The grazing angle of the incident waves is calculated using

$$h = \frac{\hat{u}(\Delta z)\hat{u}^*(-\Delta z)}{\left|\hat{u}(\Delta z)\right|\left|\hat{u}(-\Delta z)\right|}$$
$$\theta_l = \frac{1}{2k\Delta z}\tan^{-1}\left(\frac{\mathrm{Im}(h)}{\mathrm{Re}(h)}\right) \qquad (4.28)$$

The grazing angle derived using equation (4.28) may be used with a model for clutter reflectivity to give an indication of the expected backscattered clutter level. In order to check that it corresponds to the real grazing angle with a flat Earth and no atmosphere, the value modified refractivity (m in equation (4.18)) is set to zero. The results are plotted in figures 13 and 14. Figure 13 shows that the removal of m has, as expected, straightened out the interference fringes compared with the curvature evident in figure 12. Figure 14 shows that the derived grazing angle approximately follows the ray grazing angle out to 0.07° (80 km range).

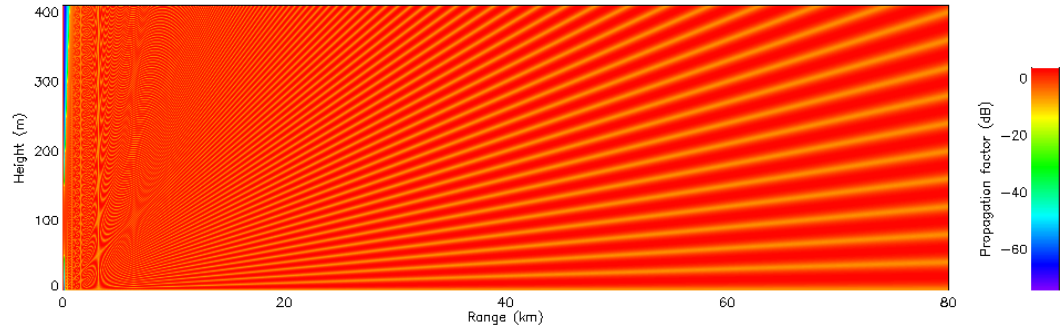

Figure 13: *Propagation factor versus range and height for an antenna height of 100m, 3GHz RF frequency, a flat Earth and no atmosphere*

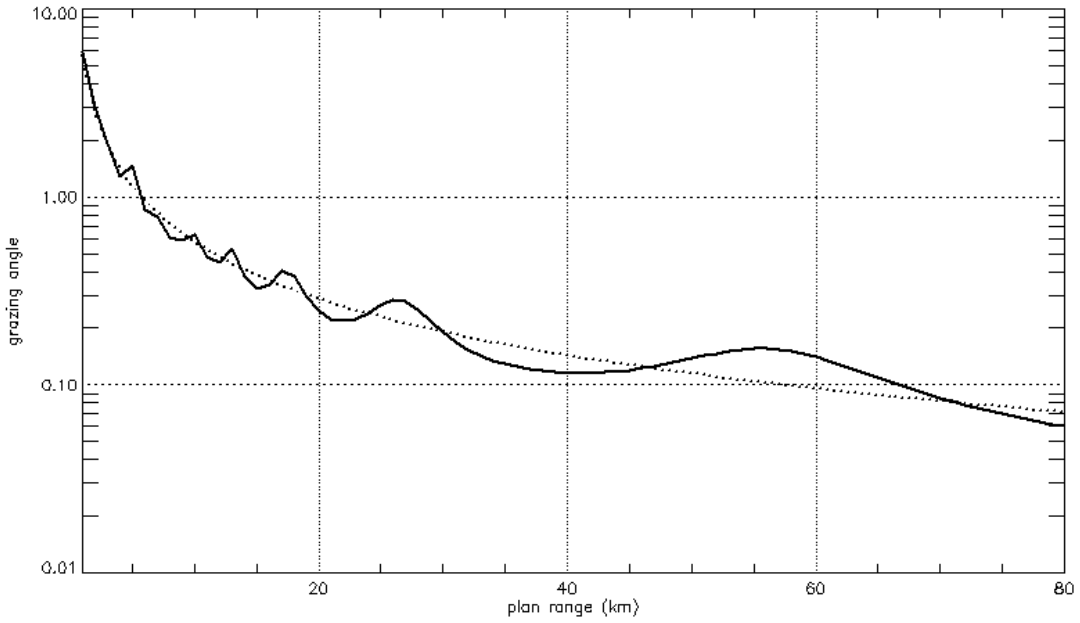

Figure 14: *Grazing angle versus range. The solid line is obtained from the data in Figure 13 using equation (4.28), the dotted line is a ray calulation.*

When the curved Earth and standard atmosphere are reintroduced the results are figure 15 and 15. These show that the derived grazing angle from equation (4.28) follows the ray value down to about 0.05° and then stays at about 0.03° out to and beyond the horizon. The ray value goes to zero at the horizon.

It is not clear why the plateau takes this value. There are non-zero EM fields in the shadow beyond the horizon and it is therefore possible to remove all waves in an upward direction and to calculate the change of phase with height, as prescribed in equation (4.28). However, it does not seem reasonable to interpret this result as an incoming plane wave for the purposes of scattering calculations. More work is required to solve the surface integral equations as described in section 4.2, but for the incoming fields derived from the propagation calculations derived here, close to, and beyond, the horizon.

In the mean time, the value of the grazing angle plateau near the horizon seems to be too small to serve as an explanation for the higher than predicted reflectivity at low grazing angles in the Nathanson tables, RRE model and NRL model.

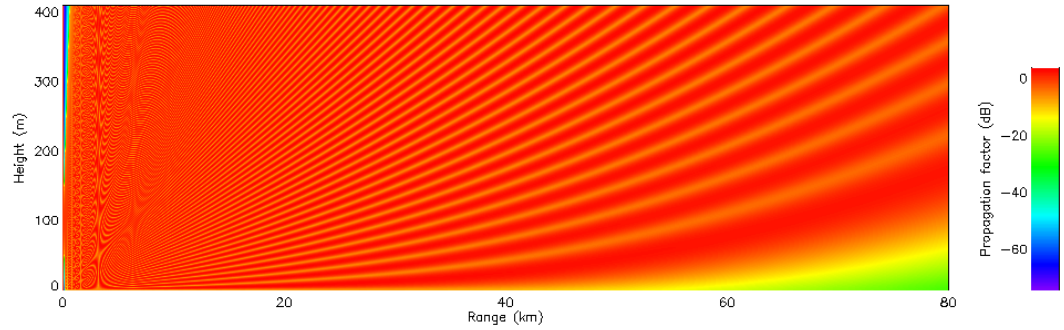

Figure 15: *Propagation factor versus range and height for an antenna height of 100m, 3GHz RF frequency, a curved Earth and a standard atmosphere*

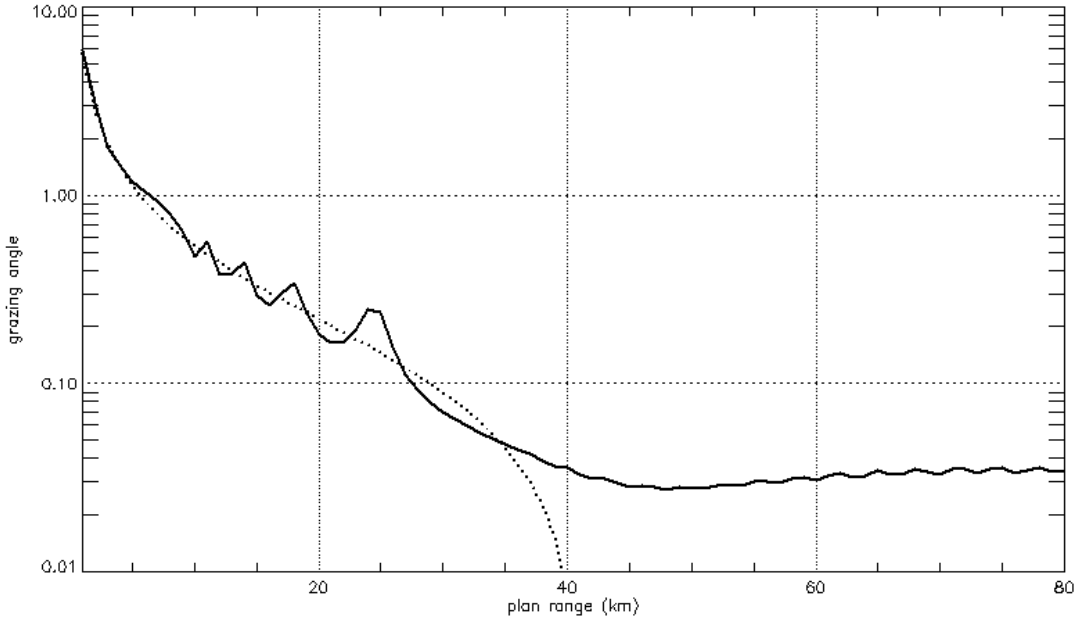

Figure 16: *Grazing angle versus range. The solid line is obtained from the data in Figure 15 using equation (4.28), the dotted line is a ray calulation assuming a 4/3 radius curved Earth.*

4.4 Consistency of reflectivity models with Sea clutter spikiness

As discussed in section 4.1, our work on sea clutter [5] has principally been concerned with fluctuation statistics. We analysed a hundred or so sea clutter measurements at X band, fitted them to K distributions and examined the variation of the shape parameter, ν, as a function of grazing angle, radar resolution, sea state and polarisation.

This led to an empirical model for the average dependence of ν on radar, environmental and geometric parameters:

$$\log_{10}(\nu) = \frac{2}{3}\log_{10}\left(\phi_{gr}^{o}\right) + \frac{5}{8}\log_{10}(A_c) - k_{pol} - \frac{\cos(2\theta_{sw})}{3} \qquad (4.29)$$

where ϕ_{gr}^{o} is the grazing angle in degrees

A_c is the radar resolved area (square metres)

k_{pol} is a polarisation dependent parameter (1.39 for VV and 2.09 for HH), and

θ_{sw} is the aspect angle with respect to the swell direction

(The last term is omitted if there is no swell)

From this model we see that, all other things being equal, ν varies as grazing angle to the power 2/3. We can measure the effect of ν on the relative RCS of the largest spikes to the mean clutter reflectivity by examining the probability of exceeding a threshold for the K distribution. Figure 17 shows the thresholds (relative to the clutter mean power) that are required to obtain three false alarm probabilities, plotted versus the K distribution shape parameter ν. The plot shows that in spiky clutter (small ν) a reduction by a factor of 10 in ν results in the 'largest spikes to mean clutter level' increasing by about 8.5 dB. Using the empirical model equation (4.29), figure 17 implies that in order for the spikes to remain at the same absolute RCS as the grazing angle changes, the reflectivity would need to reduce by 8.5 * (2/3) = 5.7 dB when the grazing angle is reduced by a factor of 10.

It would be difficult to envisage a physical model that resulted in spike RCS increasing without bound as the grazing angle reduced. However, all of the potential reflectivity models considered here satisfy the criterion of at least a 5.7 dB reduction in reflectivity for an asymptotic decrease of a factor of 10 in grazing angle. Therefore they are all consistent with the spikiness model at that level.

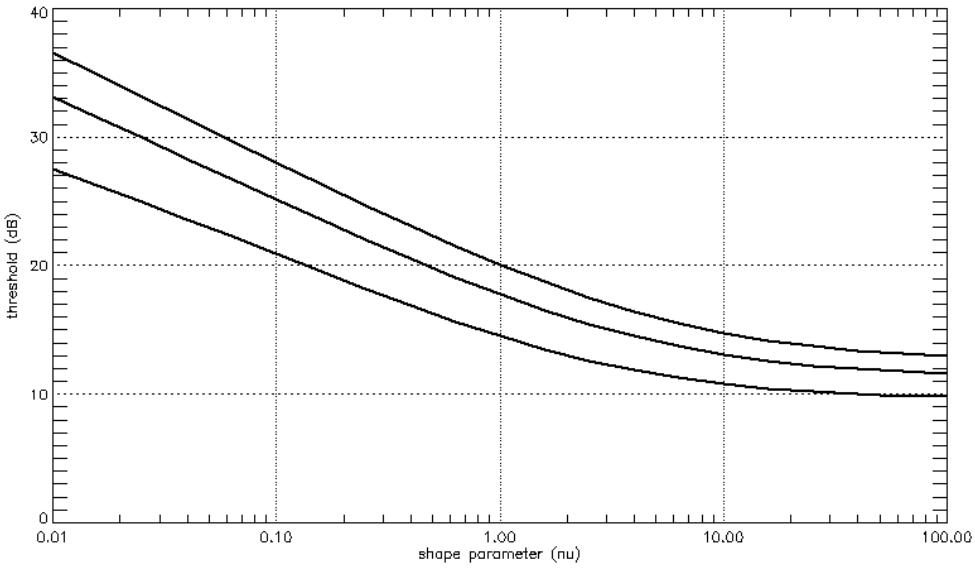

Figure 17: *Threshold (relative to mean clutter power) required to obtain false alarm probabilities of 10^{-4} (lower curve), 10^{-6} (middle curve) and 10^{-8} (upper curve) versus shape parameter for a K distribution.*

5. Measurement accuracy with multistatic radar

One potential benefit of multistatic radar systems is their ability to locate and track targets more accurately than equivalent monostatic systems. However, quantification and analysis of this benefit is generally very complicated and mathematical. In order to allow straightforward comparisons to be made, a simple method of deriving the accuracies using Gaussian error modelling and techniques similar to those used in the derivation and application of Kalman filters is described below.

The determination of the position of a target, subject to measurement noise, is equivalent to determining the mean of the distribution of a random process from a set of realisations of that process. It is practically convenient, and physically reasonable, to adopt a Gaussian model for the process. Measurements of the target's position from a single sensor can therefore be modelled by the determination of the mean of a Gaussian process. As is well known this can be done quite simply by forming the arithmetic mean of a set of independent samples of the process. Determining a single target's position from the outputs of two sensors with different error characteristics is analogous to determining the common mean of two Gaussian processes with the same mean, but different standard deviation. How do we adapt the simple procedure for determining the mean of a single process to this case?

A systematic approach to this problem, which contains the determination of the mean of a single Gaussian as a special case and allows us to take account of the different sensor error statistics in the general case, can be derived from Bayes' theorem. Merely stating this theorem tends to belie the power of its application, through the quantification of the inference process, to determining the parameters characterising the PDF which we take as the model of the data whose values we are measuring. In the simple case of a single Gaussian process these are the mean *a* and variance σ^2 of the data $\{x_i\}$ with the assumed PDF

$$P(x_i \mid a,\sigma^2) = \frac{1}{\sqrt{2\pi\sigma^2}} \exp\left(-\frac{(x_i - a)^2}{2\sigma^2}\right) \tag{5.1}$$

If we know the values of *a* and σ^2 we can characterise those of the $\{x_i\}$; if we assume that a measure of the credence placed in the values of *a* and σ^2 on the basis of the measurements $\{x_i\}$ satisfy the so-called Cox axioms we are able to treat these values of *a* and σ^2 as if they too are random variables which have a joint PDF, along with the data, which we write as $P(\{x_i\},a,\sigma^2)$. This in turn can be written in terms of conditional and marginal probabilities

$$P(\{x_i\},a,\sigma^2) = P(\{x_i\} \mid a,\sigma^2)P(a,\sigma^2) = P(a,\sigma^2 \mid \{x_i\})P(\{x_i\}) \tag{5.2}$$

Thus we can write the conditional probability that the mean and variance take the values *a* and σ^2, given that the data described by the Gaussian model take values $\{x_i\}$, as

$$P(a,\sigma^2 \mid \{x_i\}) = \frac{P(\{x_i\} \mid a,\sigma^2)P(a,\sigma^2)}{P(\{x_i\})} = \frac{P(\{x_i\} \mid a,\sigma^2)P(a,\sigma^2)}{\int da d\sigma^2 P(\{x_i\} \mid a,\sigma^2)P(a,\sigma^2)} \tag{5.3}$$

The marginal probability $P(a,\sigma^2)$ incorporates our prior knowledge of the values the parameters might take. If, for example we know the value of the variance *a priori* the marginal probability will contain a delta function that fixes this value. In circumstances of less certainty $P(a,\sigma^2)$ term is frequently ignored and the conditional probability $P(a,\sigma^2 \mid \{x_i\})$ is taken to be proportional to the likelihood $P(\{x_i\} \mid a,\sigma^2)$. Thus, given the data $\{x_i\}$ we can identify the values of the mean and variance that we are able to infer most strongly from that data as those that maximise the likelihood $P(\{x_i\} \mid a,\sigma^2)$.

We consider the case where the measured quantities are *x* and *y* with PDFs with identical means and different variances

$$P(x \mid a) = \frac{1}{\sqrt{2\pi\sigma_x^2}} \exp\left(-\frac{(x-a)^2}{2\sigma_x^2} \right) \quad P(y \mid a) = \frac{1}{\sqrt{2\pi\sigma_y^2}} \exp\left(-\frac{(y-a)^2}{2\sigma_y^2} \right) \tag{5.4}$$

The PDF of *a*, conditional on the two data points drawn from the separate distributions takes the form

$$P(a \mid x, y) \propto \exp\left(-\frac{(x-a)^2}{2\sigma_x^2} - \frac{(y-a)^2}{2\sigma_y^2} \right) \tag{5.5}$$

The exponent in this expression can be re-arranged as follows

$$\begin{aligned} \frac{(x-a)^2}{2\sigma_x^2} + \frac{(y-a)^2}{2\sigma_y^2} &= \frac{1}{2\sigma_x^2\sigma_y^2}\left(\sigma_y^2(x-a)^2 + \sigma_x^2(y-a)^2 \right) \\ &= \frac{1}{2\sigma_x^2\sigma_y^2}\left(\left(\sigma_x^2 + \sigma_y^2\right)a^2 - 2a\left(\sigma_y^2 x + \sigma_x^2 y\right) + \sigma_y^2 x^2 + \sigma_x^2 y^2 \right) \\ &= \frac{1}{2\sigma_x^2\sigma_y^2}\left(\left(\sigma_x^2 + \sigma_y^2\right)\left(a - \frac{y\sigma_x^2 + x\sigma_y^2}{\sigma_x^2 + \sigma_y^2} \right)^2 + \frac{\sigma_x^2\sigma_y^2(x-y)^2}{\sigma_x^2 + \sigma_y^2} \right) \end{aligned} \tag{5.6}$$

so that

$$P(a \mid x, y) \propto \exp\left(-\frac{1}{2}\left(\left(\frac{1}{\sigma_x^2} + \frac{1}{\sigma_y^2} \right)\left(a - \frac{y\sigma_x^2 + x\sigma_y^2}{\sigma_x^2 + \sigma_y^2} \right)^2 + \frac{(x-y)^2}{\sigma_x^2 + \sigma_y^2} \right) \right) \tag{5.7}$$

Thus we see that the estimate that maximises the likelihood is

$$\hat{a}_1 = \frac{x_1\sigma_y^2 + y_1\sigma_x^2}{\sigma_y^2 + \sigma_x^2} \tag{5.8}$$

This estimate takes account of our knowledge of how much noise is present in the measurements of x and y, assigning more weight to the less corrupted measurement.

In this simple case we see that we can combine the estimates of *a* based on the separate values of *x* and *y* to give the best estimate from the two sets in a way that is quite sensible in physical terms. It is interesting to note that the arguments we use here are very similar to, albeit rather simpler than, those that provide the basis for sequential estimation and Kalman filtering techniques.

We now extend this approach to the multi-variable case, where the measurements are of the vectors **x** and **y**, These of each has the mean **a**, the errors in the separate measurements are characterised by their associated, and different, covariance matrices $\mathbf{K}_x, \mathbf{K}_y$. The likelihood can then be constructed as

$$P(\mathbf{x}, \mathbf{y} \mid \mathbf{a}) \propto P(\mathbf{a} \mid \mathbf{x}, \mathbf{y}) \propto \exp\left(-\frac{1}{2}\left[(\mathbf{x}-\mathbf{a})^{\mathrm{T}} \cdot \mathbf{K}_x^{-1} \cdot (\mathbf{x}-\mathbf{a}) + (\mathbf{y}-\mathbf{a})^{\mathrm{T}} \cdot \mathbf{K}_y^{-1} \cdot (\mathbf{y}-\mathbf{a}) \right] \right) \tag{5.9}$$

The exponent in this expression can be recast into the form

$$
\begin{aligned}
&(\mathbf{x}-\mathbf{a})^{\mathrm{T}}\cdot\mathbf{K}_x^{-1}\cdot(\mathbf{x}-\mathbf{a})+(\mathbf{y}-\mathbf{a})^{\mathrm{T}}\cdot\mathbf{K}_y^{-1}\cdot(\mathbf{y}-\mathbf{a})= \\
&(\mathbf{a}-\mathbf{m})^{\mathrm{T}}\cdot\left(\mathbf{K}_x^{-1}+\mathbf{K}_y^{-1}\right)\cdot(\mathbf{a}-\mathbf{m})-\mathbf{m}^{\mathrm{T}}\cdot\left(\mathbf{K}_x^{-1}+\mathbf{K}_y^{-1}\right)\cdot\mathbf{m}+\mathbf{x}^{\mathrm{T}}\cdot\mathbf{K}_x^{-1}\cdot\mathbf{x}+\mathbf{y}^{\mathrm{T}}\cdot\mathbf{K}_y^{-1}\cdot\mathbf{y} \\
&\mathbf{m}=\left(\mathbf{1}+\mathbf{K}_x\cdot\mathbf{K}_y^{-1}\right)^{-1}\cdot\mathbf{x}+\left(\mathbf{1}+\mathbf{K}_y\cdot\mathbf{K}_x^{-1}\right)^{-1}\cdot\mathbf{y}=\left(\mathbf{K}_x^{-1}+\mathbf{K}_y^{-1}\right)^{-1}\cdot\left(\mathbf{K}_x^{-1}\cdot\mathbf{x}+\mathbf{K}_y^{-1}\cdot\mathbf{y}\right)
\end{aligned}
\tag{5.10}
$$

Thus we have

$$
P(\mathbf{a}\mid\mathbf{x},\mathbf{y})\propto\exp\left(-\frac{1}{2}\left[(\mathbf{a}-\mathbf{m})^{\mathrm{T}}\cdot\left(\mathbf{K}_x^{-1}+\mathbf{K}_y^{-1}\right)\cdot(\mathbf{a}-\mathbf{m})\right]\right) \tag{5.11}
$$

The usual likelihood maximisation argument has us identify the estimate of **a** as

$$
\hat{\mathbf{a}}=\mathbf{m} \tag{5.12}
$$

The extension to m sensors, each making a measurement of the same mean value **a** but with a different error covariance matrix $\mathbf{K}(j),\quad 1\le j\le m$, is quite straightforward and yields

$$
\hat{\mathbf{a}}=\left(\sum_{j=1}^{m}\mathbf{K}^{-1}(j)\right)^{-1}\cdot\left(\sum_{i=1}^{m}\mathbf{K}^{-1}(i)\cdot\mathbf{x}(i)\right) \tag{5.13}
$$

The mean of this estimate can be evaluated as

$$
\left\langle\hat{\mathbf{a}}\right\rangle=\left(\sum_{j=1}^{m}\mathbf{K}^{-1}(j)\right)^{-1}\cdot\left(\sum_{i=1}^{m}\mathbf{K}^{-1}(i)\cdot\left\langle\mathbf{x}(i)\right\rangle\right)=\left(\sum_{j=1}^{m}\mathbf{K}^{-1}(j)\right)^{-1}\cdot\left(\sum_{i=1}^{m}\mathbf{K}^{-1}(i)\cdot\mathbf{a}\right)=\mathbf{a} \tag{5.14}
$$

while its covariance matrix can be calculated directly as

$$
\begin{aligned}
&\left\langle(\hat{\mathbf{a}}-\mathbf{a})(\hat{\mathbf{a}}-\mathbf{a})^{\mathrm{T}}\right\rangle=\left(\sum_{j=1}^{m}\mathbf{K}^{-1}(j)\right)^{-1}\cdot\left\langle\left(\sum_{i=1}^{m}\mathbf{K}^{-1}(i)\cdot(\mathbf{x}(i)-\mathbf{a})\right)\left(\sum_{j=1}^{m}\mathbf{K}^{-1}(j)\cdot(\mathbf{x}(j)-\mathbf{a})\right)^{\mathrm{T}}\right\rangle\cdot\left(\sum_{j=1}^{m}\mathbf{K}^{-1}(j)\right)^{-1} \\
&=\left(\sum_{j=1}^{m}\mathbf{K}^{-1}(j)\right)^{-1}\cdot\left(\sum_{i=1}^{m}\mathbf{K}^{-1}(i)\cdot\left\langle(\mathbf{x}(i)-\mathbf{a})(\mathbf{x}(i)-\mathbf{a})^{\mathrm{T}}\right\rangle\cdot\mathbf{K}^{-1}(i)\right)\cdot\left(\sum_{j=1}^{m}\mathbf{K}^{-1}(j)\right)^{-1} \\
&=\left(\sum_{j=1}^{m}\mathbf{K}^{-1}(j)\right)^{-1}\cdot\left(\sum_{i=1}^{m}\mathbf{K}^{-1}(i)\cdot\mathbf{K}(i)\cdot\mathbf{K}^{-1}(i)\right)\cdot\left(\sum_{j=1}^{m}\mathbf{K}^{-1}(j)\right)^{-1}=\left(\sum_{j=1}^{m}\mathbf{K}^{-1}(j)\right)^{-1}
\end{aligned}
\tag{5.15}
$$

as we would expect from our two variable special case (5.11). As the estimator is a Gaussian variable this mean and covariance are all we need to determine its single point statistics.

Equations (5.13) and (5.15) show that estimation of the vector **a** (which in multi-static radar can be either a target's position or its velocity vector) and the accuracy of this estimation depend only upon the *inverse* of the covariance matrices of the individual measurement errors. Therefore, when only a single component of a vector is measured (eg the range rate of a target) by a transmitter-receiver pair, the inverse of the 3D error covariance can be specified by setting the inverse error of the unmeasured components to zero. The inverse covariance matrices from all the multi-static channels can be rotated (without inverting them) to the same coordinate system and then summed to evaluate (5.13) and (5.15) in a straightforward manner.

References

1. Report on Scattering Physics of Multistatic Radar Sea clutter, Oct 2011 to Sept 2012.

2. Vilhelm Gregers-Hansen and Rashmi Mital, *'An improved Empirical model for Radar Sea Clutter Reflectivity'*, NRL report NRL/MR/5310-12-9346, April 2012

3. F. E. Nathanson, J. P. Reilly, and M. Cohen, *Radar Design Principles*, 2 edition. New York: McGraw-Hill, 1991.

4. *'RRE σ_0 sea clutter model'*, Royal Radar Establishment, 1974 (unpublished).

5. KD Ward, RJA Tough and S Watts, 'Sea Clutter: Scattering, the K Distribution and Radar Performance', First Edition, IET London 2006.

6. M. Horst, F. Dyer, M. Tuley, *'Radar sea clutter model'*, Int IEEE AP/S URSI Symposium (IEEE Antennas and Propagation), 1978

7. D. Holliday, L.L. DeRaad, Jr. and G.J. St.-Cyr, '*Forward-backward: a new method for computing low grazing angle scattering*.', IEEE Trans. Antennas and Propagation, **44**, 722-729, 1996

8. KD Ward, RJA Tough and S Watts, 'Sea Clutter: Scattering, the K Distribution and Radar Performance', Second Edition chapter 15, IET London 2013.

9. Recommendation ITU-R P.453-10, "*The radio refractive index: its formula and refractivity data*", 02/2012

10. V A Fock, Diffraction, refraction and reflection of radio waves: Thirteen papers by V. A. Fock, AFCRD-TN-57-102 ASTIA Document No AD117276, 1987

11. James Branson, "*Propagation modelling for the analysis of radar systems*", Phd Thesis, UCL, 2008

12. M Levy, "Parabolic equation methods for electromagnetic wave propagation", IEE Electromagnetic Waves Series 45, 2000

13. J P Zhang et al, *"Evaporation Duct Retrieval Using Changes In Radar Sea Clutter Power Versus Receiving Height*", Progress in Electromagnetics Research, Vol 126, 2012